Editors' Suggestion **Featured in Physics**

Interrelated Thermalization and Quantum Criticality in a Lattice Gauge Simulator

Han-Yi Wang,[1,*] Wei-Yong Zhang,[1,*] Zhiyuan Yao,[2,3,*] Ying Liu,[1] Zi-Hang Zhu,[1] Yong-Guang Zheng,[1]
Xuan-Kai Wang,[1] Hui Zhai,[3,4] Zhen-Sheng Yuan,[1,4,5] and Jian-Wei Pan[1,4,5]
[1]*Hefei National Research Center for Physical Sciences at the Microscale and School of Physical Sciences, University of Science and Technology of China, Hefei 230026, China*
[2]*Key Laboratory of Quantum Theory and Applications of MoE, Lanzhou Center for Theoretical Physics, and Key Laboratory of Theoretical Physics of Gansu Province, Lanzhou University, Lanzhou, Gansu 730000, China*
[3]*Institute for Advanced Study, Tsinghua University, Beijing 100084, China*
[4]*Hefei National Laboratory, Hefei 230088, China*
[5]*CAS Center for Excellence in Quantum Information and Quantum Physics, University of Science and Technology of China, Hefei 230026, China*

(Received 8 December 2022; accepted 22 June 2023; published 1 August 2023)

Gauge theory and thermalization are both topics of essential importance for modern quantum science and technology. The recently realized atomic quantum simulator for lattice gauge theories provides a unique opportunity for studying thermalization in gauge theory, in which theoretical studies have shown that quantum thermalization can signal the quantum phase transition. Nevertheless, the experimental study remains a challenge to accurately determine the critical point and controllably explore the thermalization dynamics due to the lack of techniques for locally manipulating and detecting matter and gauge fields. We report an experimental investigation of the quantum criticality in the lattice gauge theory from both equilibrium and nonequilibrium thermalization perspectives, with the help of the single-site addressing and atom-number-resolved detection capabilities. We accurately determine the quantum critical point and observe that the Néel state thermalizes only in the critical regime. This result manifests the interplay between quantum many-body scars, quantum criticality, and symmetry breaking.

DOI: 10.1103/PhysRevLett.131.050401

Introduction.—Since quantum gauge theories are computationally intractable in the nonperturbative regime, the idea of formulating gauge theories on discretized spacetime lattices led to lattice gauge theories (LGTs) [1], and the developments of LGTs enabled numerical simulation of gauge theories with various classical algorithms in the past decades [2,3]. Recently, a new trend is realizing LGTs in quantum simulators with ultracold atoms or trapped ions [4–9]. By taking the quantum advantage, these quantum simulation platforms offer the promise of a better understanding of LGTs than classical simulations [10–15].

One potential advantage of quantum simulation for studying LGTs lies in the nonequilibrium dynamics, such as quantum thermalization [16–18]. In ultracold atom systems, the essential parameters in the gauge theory are tunable, allowing accessing different phases and the quantum criticality in between. Quantum criticality refers to a qualitative change of the ground state and the universal behavior of low-energy physics. On the contrary, thermalization dynamics usually involves highly excited states. Remarkably, it has been recently proposed that the thermalization dynamics of the Néel state (labeled as $|\mathbb{Z}_2\rangle$) can also signal the quantum critical regime in the U(1) LGT [19,20]. However, it is challenging to study these physics due to the lack of techniques for manipulating and detecting local matter and gauge fields in the previous experiments.

In this Letter, we report on an experimental study of both equilibrium and thermalization dynamics in the quantum critical regime of the U(1) LGT. We integrate the techniques of single-site manipulation of matter and gauge fields and atom-number-resolved detection into an updated LGT simulator. With these technical advances, we can monitor the local Gauss law and then perform the postselection, which eliminates the processes violating local gauge symmetries. We can measure the order parameter with various system sizes to perform a proper finite-size scaling, which overcomes the finite-size effects and determines the critical point accurately. We can also deterministically prepare the $|\mathbb{Z}_2\rangle$ state by addressing single atoms in a programmed manner. Equipped with these capabilities, we observe the nontrivial thermalization dynamics across the quantum critical regime [19,20].

Experimental setup.—Our experimental system is shown in Fig. 1(a), which realizes a U(1) LGT using bosons in optical lattices, and the protocol is the same as that reported in previous work [8]. We combine a short lattice and a long lattice with twice the lattice spacing to create a one-dimensional superlattice, and this superlattice contains alternating deep and shallow lattice sites, as shown in Fig. 1(b) [26]. When the deep lattice sites are doubly occupied, the on-site energy is $U - 2\delta$, where U is the

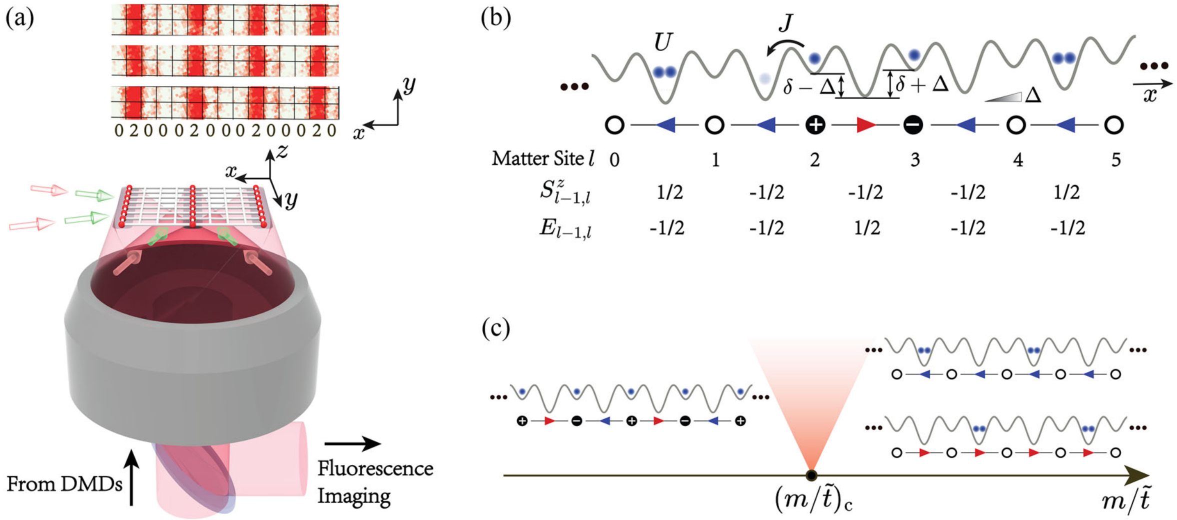

FIG. 1. Experimental system. (a) Schematic of the ultracold atom microscope and the prepared $|\mathbb{Z}_2\rangle$ initial state. We combine the optical superlattices and the addressing beam generated by the digital micromirror device (DMD) to prepare the initial $|\mathbb{Z}_2\rangle$ state [21]. The top shows an exemplary raw-data fluorescence image of the atom distribution of the initial $|\mathbb{Z}_2\rangle$ state in a single experimental realization. (b) The physical model with bosons in a one-dimensional optical lattice with alternating deep and shallow lattice sites. Here, U denotes the on-site interaction strength, J denotes the hopping amplitude of bosons, δ denotes the energy offset between neighboring shallow and deep lattices, and Δ denotes the linear tilt per site. The open and solid circles with + or − denote physical charge zero, +1 or −1 at the matter sites, and the arrows denote the electric field. (c) An Ising-type quantum phase transition by tuning $m/\tilde{t}$.

on-site interaction energy and δ is the energy offset between deep and shallow lattices. When $U \approx 2\delta$, the on-site energy of a doubly occupied site is nearly degenerate with an empty site, but is off-resonant with a singly occupied state. Thus, we only retain the empty and doubly occupied states, denoted by $|\downarrow\rangle$ and $|\uparrow\rangle$, respectively. These deep lattice sites are viewed as gauge sites, and the shallow lattice sites are viewed as matter sites. This realizes the LGT written as [8,21]

$$\hat{H} = \sum_l [\tilde{t}(\hat{\psi}_l \hat{S}^+_{l,l+1} \hat{\psi}_{l+1} + \text{H.c.}) + m\hat{\psi}^\dagger_l \hat{\psi}_l], \tag{1}$$

where l labels the matter sites and $\hat{\psi}_l$ are bosonic operators for the matter fields. Spin-1/2 operators $\hat{S}_{l,l+1}$ are defined in the deep lattices. Here $m = \delta - U/2$ is the mass of the matter field. $\tilde{t}$ is generated by a second-order hopping process because the long-range direct hoppings are suppressed by applying a tilting potential.

This model possesses local gauge symmetries because the Hamiltonian Eq. (1) is invariant under the local gauge transformation that individually rotates the $\hat{\psi}_l$ operator at each site as $\hat{\psi}_l \to e^{i\theta_l}\hat{\psi}_l$, and correspondingly, the spin operators are changed as $\hat{S}^+_{l,l+1} \to e^{-i\theta_l - i\theta_{l+1}}\hat{S}^+_{l,l+1}$ and $\hat{S}^+_{l-1,l} \to e^{-i\theta_{l-1} - i\theta_l}\hat{S}^+_{l-1,l}$ [8]. This local gauge symmetry gives rise to a set of local conserved quantities $G_l = S^z_{l-1,l} + S^z_{l,l+1} + n_l$. By introducing the electric field $E_{l-1,l} = (-1)^l S^z_{l-1,l}$ and the physical charge $Q_l = (-1)^l n_l$, the conservation $G_l = 0$ can be written as

$$E_{l,l+1} - E_{l-1,l} = Q_l, \tag{2}$$

which is exactly the Gauss law of U(1) LGTs [8]. A configuration of the electric field and Gauss law is also schematically shown in Fig. 1(b).

When focusing on the gauge sector with all $G_l = 0$, there are two phases in the Hamiltonian Eq. (1) as tuning $m/\tilde{t}$. This can be easily seen by looking at two limits with $m/\tilde{t} = \pm\infty$. When $m/\tilde{t} \to +\infty$, the matter field favors $n_l = 0$ and therefore $S^z_{l-1,l} + S^z_{l,l+1} = 0$, leading to an antiferromagnetic state $|\mathbb{Z}_2\rangle = |\uparrow\downarrow\uparrow\downarrow\ldots\rangle$ or $|\downarrow\uparrow\downarrow\uparrow\ldots\rangle$ at gauge sites. This leads to a twofold degenerate ground state. When $m/\tilde{t} \to -\infty$, the matter field favors $n_l = 1$ and therefore $S^z_{l-1,l} = S^z_{l,l+1} = -1/2$. This state does not break the original lattice translational symmetry. Hence the transition is a Z_2 symmetry breaking transition of the Ising type, and detailed theoretical calculations predict the critical point at $m/\tilde{t} \approx 0.655$ [27–29]. Signatures of two different phases have also been observed in the previous experiment [8]. However, the absorption imaging detection method used there lacks single-site resolution, preventing an accurate determination of the critical point.

Adiabatic ramping.—To accurately determine the quantum critical point, we first prepare a $|\mathbb{Z}_2\rangle$ state with high fidelity utilizing the ability of single-site addressing [21] at $\delta = 447(1)$ Hz, $U = 732(2)$ Hz, and $\tilde{t} = 23.5(2)$ Hz, corresponding to $m/\tilde{t} = 3.44(7)$ [30]. This $|\mathbb{Z}_2\rangle$ state is an antiferromagnetic state $|\uparrow\downarrow\uparrow\downarrow\ldots\rangle$ in the gauge sites and empty sites in the matter sites. Here, we prepare 5–10 copies of identical chains along the x direction, as shown in Fig. 1(a). Each chain contains L gauge sites and $L + 1$ matter sites, with a total of $L + 1$ atoms in each chain. Here

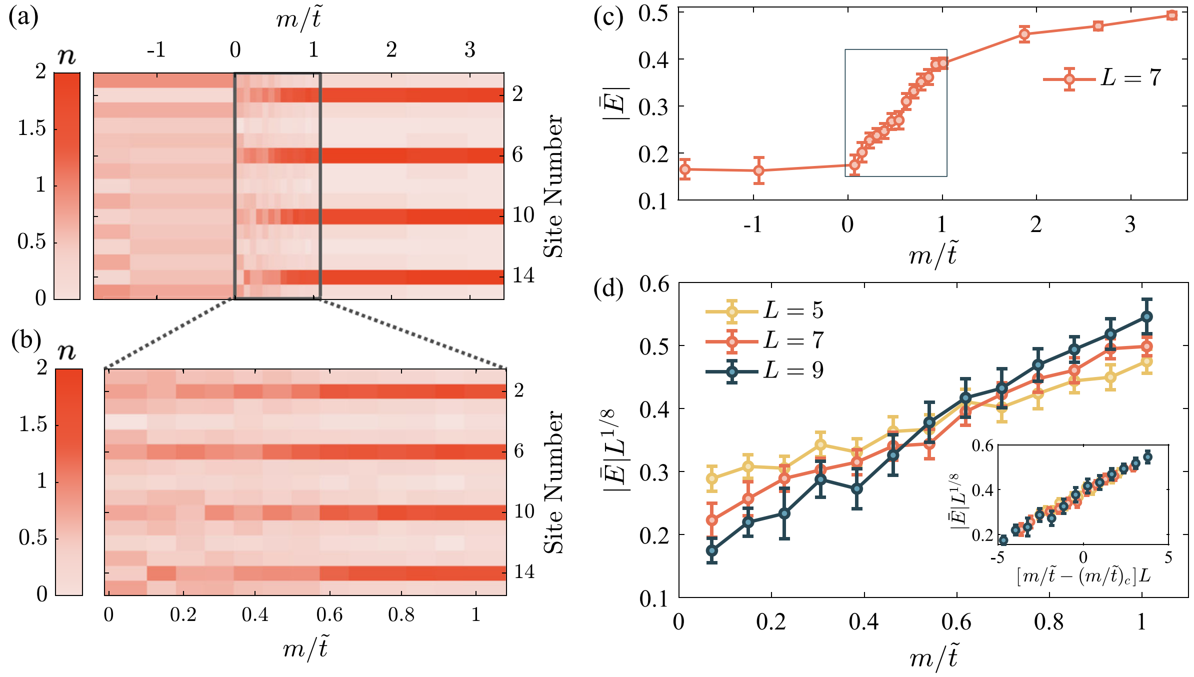

FIG. 2. Adiabatic ramping and phase transition. (a),(b) Single-site-resolved atom number distribution for a range of $m/\tilde{t}$. (c) The absolute of the spatial averaged electric field $|\bar{E}|$ as a function of $m/\tilde{t}$. (d) $|\bar{E}|L^{1/8}$ as a function of $m/\tilde{t}$ for $L = 5, 7, 9$. The crossing point of the three curves locates the quantum critical point. The inset verifies the critical behavior by showing $|\bar{E}|L^{\beta/\nu}$ plotted against $[m/\tilde{t} - (m/\tilde{t})_c]L^{1/\nu}$, which collapse onto a single curve near the critical point [33,34]. Error bars denote the standard error of the mean.

we choose $L = 5, 7, 9$ that is convenient for deterministic state preparation. Then, we adiabatically ramp δ to the targeted critical regime around 373 Hz, with a constant ramping speed $\dot{\delta} = 2.1$ Hz/ms. Such change of δ leaves U and $\tilde{t}$ nearly unaffected, and it changes the value of $m/\tilde{t}$ to the critical regime, as shown in Fig. 2. Finally, the system is suddenly frozen and the atom number at each site is read out with the single-site-resolved microscope. Note that usually the fluorescence imaging cannot distinguish two atoms from zero atom at the same site [31,32]. Here, before detection, we split two atoms into two sites of a double well along the y direction if there are two atoms at the same site. This allows us to resolve atom number two from zero at a single site [21]. To mitigate the undesired effects from processes beyond the LGT, we postselect our data based on two rules: (i) the total atom number remains the same as that of the initial state and (ii) the Gauss law Eq. (2) has to be obeyed for all sites. In our case, about 60% of total images are discarded [21]. With the adiabatic ramping and the postselection, we ensure that the ground state of the LGT at the targeted $m/\tilde{t}$ is reached. The results of single-site-resolved measurement of atom number distribution is shown in Fig. 2(a) for a range of $m/\tilde{t}$.

To locate the critical point, we measure the order parameter $L^{-1}\sum_l(-1)^l S^z_{l-1,l}$. This order parameter is the staggered magnetization, and given the definition of the electric field, this order parameter is also the spatial averaged electric field strength, denoted by $\bar{E}$. We plot $|\bar{E}|$ as a function of $m/\tilde{t}$ with $L = 7$ in Fig. 2(c), which exhibits a rapid change when $m/\tilde{t}$ is in the range $\sim[0, 1]$. The finite-size scaling theory predicts that nearby the critical point, $|\bar{E}|L^{\beta/\nu}$ is a universal function of $[m/\tilde{t} - (m/\tilde{t})_c]L^{1/\nu}$ [33,34]. For the two-dimensional Ising universality class, the order parameter critical exponent $\beta = 1/8$ and the correlation length critical exponent $\nu = 1$ [35]. To more accurately determine the critical point, we perform a finite-size scaling using data in this range. We plot $|\bar{E}|L^{\beta/\nu}$ as a function of $m/\tilde{t}$ for different system size $L = 5, 7, 9$. The crossing point of these curves locates the critical point [21]. Here we indeed observe the crossing of three curves. However, since each data point has an error bar, it is not clear to visualize the exact crossing point. Hence, we consider each point as a normalized Gaussian distribution $p_i(x) = \mathcal{N}(\mu_i, \sigma_i^2)$, where $x = |\bar{E}|L^{1/8}$, μ_i and σ_i are, respectively, the value and the error bar of each data point. We calculate the averaged Kullback–Leibler (KL) divergence of the three Gaussian distributions at each $m/\tilde{t}$, which quantifies the degree of overlap between three Gaussian distributions. The averaged KL divergence is defined as [36]

$$D_{\mathrm{KL}} = \frac{1}{6}\sum_{i,j=1}^{3}\int_{-\infty}^{+\infty} dx\, p_i(x) \log\left(\frac{p_i(x)}{p_j(x)}\right). \tag{3}$$

We plot the D_{KL} as a function of $m/\tilde{t}$ in Fig. 4(a), and fitting the data yields a peak position at $m/\tilde{t} = 0.59(8)$. This value

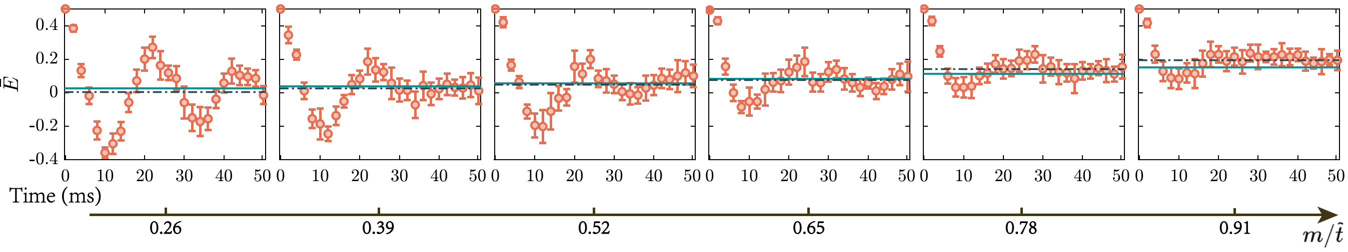

FIG. 3. Time evolution after a quench. The real-time dynamics of $\bar{E}$ for different values of $m/\tilde{t}$ (marked at the axes of $m/\tilde{t}$). The dashed lines are the fitted longtime steady values E_∞, and the solid lines are the theoretical thermal values E_{th} assuming that the initial state fully thermalizes. Here $L = 7$ and each data point is averaged over 10–20 chains after the postselection. Error bars denote the standard error of the mean, and are smaller than the markers if hidden.

is consistent with theoretical predictions [27–29]. Given the energy scale of our $\tilde{t}$, the deviation from the theoretical critical value is less than 2 Hz.

Quench dynamics.—We then consider the quench dynamics. The same $|\mathbb{Z}_2\rangle$ state is prepared as the initial state. Now, instead of adiabatic ramping, we suddenly change the value of $m/\tilde{t}$ to the targeted value nearby the critical point from $m/\tilde{t} = 10$, with a typical timescale of 1 ms. Here we fix $\tilde{t} = 34.1(3)$ Hz and $U = 676(2)$ Hz. The value of $\tilde{t}$ is larger than what we used for the adiabatic ramping process. This is because we find that even a weak spatial inhomogeneity can cause noticeable variations of m from site to site, which can affect the time dynamics. A larger $\tilde{t}$ helps to reduce this variation in terms of $m/\tilde{t}$ and can significantly suppress the effects of the inhomogeneity. We record the spatial atom number distribution at different times during the real-time dynamics using a single-site-resolved microscope. We also apply the same postselection to ensure that the dynamics is governed by the LGT. The measurements of time dynamics are shown in Fig. 3 for different values of $m/\tilde{t}$.

We fit the experimental data in Fig. 3 with a damped sinusoidal function $Ae^{-t/\tau}\sin(\omega t) + E_\infty$, where A, τ, ω, and E_∞ are all fitting parameters. We obtain E_∞ as the longtime steady value, as illustrated by the dashed lines in Fig. 3. Meanwhile, we can also theoretically extract the thermalization values E_{th}, provided that the system obeys the eigenstate thermalization hypothesis and the initial $|\mathbb{Z}_2\rangle$ state thermalizes [37–40]. E_{th} is obtained by calculating $\mathrm{Tr}[\rho(T)L^{-1}\sum_l(-1)^l S^z_{l-1,l}]$. Here $\rho(T)$ is an equilibrium density matrix of the LGT system, with the temperature T determined by matching energy $\mathrm{Tr}[\rho(T)\hat{H}] = \langle\mathbb{Z}_2|\hat{H}|\mathbb{Z}_2\rangle$ [21]. Previous work has predicted that for the PXP model, E_∞ matches E_{th} and the initial $|\mathbb{Z}_2\rangle$ state thermalizes only in the quantum critical regime [19]. These two values depart from each other away from the critical point $(m/\tilde{t})_c$. When $m/\tilde{t} > (m/\tilde{t})_c$, the ground state is twofold degenerate and the $|\mathbb{Z}_2\rangle$ state has large overlap with the ground state, and the ground state is always not thermalized. When $m/\tilde{t} < (m/\tilde{t})_c$, especially around $m/\tilde{t} = 0$, it is known that the PXP model hosts a set of many-body scar states as the

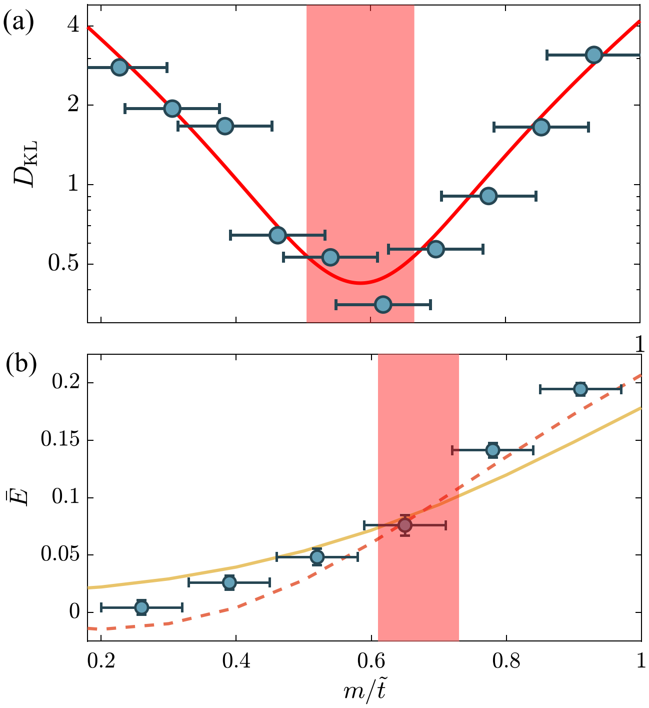

FIG. 4. Quantum criticality. (a) The averaged KL divergence D_{KL} defined by Eq. (3) quantifies the overlap of three data points for each $m/\tilde{t}$ in Fig. 2(d). D_{KL} is plotted as a function of $m/\tilde{t}$. The peak of D_{KL} defines the point where the three curves in Fig. 2(d) cross each other and locates the quantum critical point. The error bars of the data points are the error of the calibrated $m/\tilde{t}$ [21]. The determined quantum critical point $(m/\tilde{t})_c$ lies at the middle of the range of $m/\tilde{t}$ spanned by the shaded region. Its error bar (coming from both the Gaussian fitting error and the calibration error) is indicated by half of the horizontal width of the shaded region. (b) The data points are the steady values E_∞ extracted from Fig. 3. The red dashed line is the theoretical steady value with the same system size as the experimental system, and the solid yellow line is the theoretical thermal value E_{th} assuming that the initial state obeys the eigenstate thermalization hypothesis. The horizontal error bars denote the errors of the calibrated $m/\tilde{t}$, and the vertical error bars denote the standard deviations of the fitted E_∞. The center and the half width of the shaded region represent the quantum critical point (determined by the intersection between the solid yellow line and the fitted curve of the data points) and its error bar, respectively.

system's eigenstates [41–43]. The $|\mathbb{Z}_2\rangle$ state also has large overlap with the scar states, preventing it from thermalization [41–43]. The PXP model is equivalent to this LGT model under the local gauge constraints of $G_l = 0$ for all l, and therefore, the discussion also applies to this LGT model [44,45]. In Fig. 4(b), we compare E_∞ with E_{th}, and our measurements agree with the prediction that $E_\infty \approx E_{\text{th}}$ only in the quantum critical regime [19]. The numerical simulation in Ref. [19] shows that this conclusion holds in a finite system.

Conclusion.—We have performed a single-site-resolved quantitative experimental study of the quantum criticality in the U(1) LGT realized with bosons in optical lattices. Our study combines both the equilibrium property and the thermalization dynamics. To achieve single-site addressing and atom number detection while mitigating the undesirable effects of spatial inhomogeneity, our system size is up to ∼19 lattice sites. Still, our quantitative results agree well with the numerical results of exact diagonalization. This agreement benchmarks the validity of our ultracold atom quantum simulator quantitatively, and demonstrates this simulator as a powerful platform to study nonequilibrium dynamics of the gauge theory. In the near future, when our system size is enlarged several times, it will be beyond the capability of exact diagonalization. The experimental control and detection capability developed in this work can be used to study other interesting dynamical phenomena in this system, such as entanglement entropy dynamics [46,47], where the entanglement growth rate is also expected to signal the quantum criticality [21]. We can also modify our model to alter either the scar state or the symmetry breaking property, and it is expected that the thermalization behavior in different regimes should change respectively. This can help pinpoint the physical mechanism. Our system can also be used to study string breaking [48–50], dynamical transition between quantum phases [51,52], the false vacuum decay, and the confinement-deconfinement transition [44,45,53]. The current scheme of implementing the LGT can also be extended to higher dimensions [54].

We thank Meng-Da Li, Qian Xie, Bo Xiao, Hui Sun, Wan Lin, and An Luo for their help in building the experimental setup. This work was supported by NNSFC Grant No. 12125409, Innovation Program for Quantum Science and Technology 2021ZD0302000. Z. Y. also acknowledges support by NSFC Grant No. 12247101. H. Z. is also supported by the Beijing Outstanding Young Scholar Program and the XPLORER Prize.

---

[*] These authors contributed equally to this work.

[1] K. G. Wilson, Confinement of quarks, Phys. Rev. D **10**, 2445 (1974).

[2] M. C. Bañuls and K. Cichy, Review on novel methods for lattice gauge theories, Rep. Prog. Phys. **83**, 024401 (2020).

[3] H. J. Rothe, *Lattice Gauge Theories: An Introduction*, 4th ed. (World Scientific, Hackensack, NJ, 2012).

[4] E. A. Martinez, C. A. Muschik, P. Schindler, D. Nigg, A. Erhard, M. Heyl, P. Hauke, M. Dalmonte, T. Monz, P. Zoller, and R. Blatt, Real-time dynamics of lattice gauge theories with a few-qubit quantum computer, Nature (London) **534**, 516 (2016).

[5] C. Kokail, C. Maier, R. van Bijnen, T. Brydges, M. K. Joshi, P. Jurcevic, C. A. Muschik, P. Silvi, R. Blatt, C. F. Roos, and P. Zoller, Self-verifying variational quantum simulation of lattice models, Nature (London) **569**, 355 (2019).

[6] C. Schweizer, F. Grusdt, M. Berngruber, L. Barbiero, E. Demler, N. Goldman, I. Bloch, and M. Aidelsburger, Floquet approach to $\mathbb{Z}_2$ lattice gauge theories with ultracold atoms in optical lattices, Nat. Phys. **15**, 1168 (2019).

[7] A. Mil, T. V. Zache, A. Hegde, A. Xia, R. P. Bhatt, M. K. Oberthaler, P. Hauke, J. Berges, and F. Jendrzejewski, A scalable realization of local U(1) gauge invariance in cold atomic mixtures, Science **367**, 1128 (2020).

[8] B. Yang, H. Sun, R. Ott, H.-Y. Wang, T. V. Zache, J. C. Halimeh, Z.-S. Yuan, P. Hauke, and J.-W. Pan, Observation of gauge invariance in a 71-site Bose-Hubbard quantum simulator, Nature (London) **587**, 392 (2020).

[9] Z.-Y. Zhou, G.-X. Su, Jad, R. Ott, H. Sun, P. Hauke, B. Yang, Z.-S. Yuan, J. Berges, and J.-W. Pan, Thermalization dynamics of a gauge theory on a quantum simulator, Science **377**, 311 (2022).

[10] U.-J. Wiese, Ultracold quantum gases and lattice systems: Quantum simulation of lattice gauge theories, Ann. Phys. (Berlin) **525**, 777 (2013).

[11] L. Tagliacozzo, A. Celi, A. Zamora, and M. Lewenstein, Optical Abelian lattice gauge theories, Ann. Phys. (Amsterdam) **330**, 160 (2013).

[12] E. Zohar, J. I. Cirac, and B. Reznik, B. Quantum simulations of lattice gauge theories using ultracold atoms in optical lattices, Rep. Prog. Phys. **79**, 014401 (2015).

[13] M. Dalmonte and S. Montangero, Lattice gauge theory simulations in the quantum information era, Contemp. Phys. **57**, 388 (2016).

[14] M. C. Bañuls, R. Blatt, J. Catani, A. Celi, J. I. Cirac, M. Dalmonte, L. Fallani, K. Jansen, M. Lewenstein, S. Montangero, C. A. Muschik, B. Reznik, E. Rico, L. Tagliacozzo, K. Van Acoleyen, F. Verstraete, U.-J. Wiese, M. Wingate, J. Zakrzewski, and P. Zoller, Simulating lattice gauge theories within quantum technologies, Eur. Phys. J. D **74**, 165 (2020).

[15] M. Aidelsburger *et al.*, Cold atoms meet lattice gauge theory, Phil. Trans. R. Soc. A **380**, 20210064 (2022).

[16] R. M. Nandkishore and D. A. Huse, Many-body localization and thermalization in quantum statistical mechanics, Annu. Rev. Condens. Matter Phys. **6**, 15 (2015).

[17] D. A. Abanin, E. Altman, I. Bloch, and Maksym Serbyn, Many-body localization, thermalization, and entanglement, Rev. Mod. Phys. **91**, 021001 (2019).

[18] M. Ueda, Quantum equilibration, thermalization and prethermalization in ultracold atoms, Nat. Rev. Phys. **2**, 669 (2020).

[19] Z. Yao, L. Pan, S. Liu, and H. Zhai, Quantum many-body scars and quantum criticality, Phys. Rev. B **105**, 125123 (2022).

[20] C. Peng and X. Cui, Bridging quantum many-body scar and quantum integrability in Ising chains with transverse and longitudinal fields, Phys. Rev. B **106**, 214311 (2022).

[21] See Supplemental Material at http://link.aps.org/supplemental/10.1103/PhysRevLett.131.050401 for a brief derivation of the LGT studied in this Letter from the underlying Bose-Hubbard model, a detailed description of our experimental procedure, and calibrations of various experimental parameters and numerical simulation, which also includes Refs. [22–25].

[22] C. Cohen-Tannoudji, J. Dupont-Roc, and G. Grynberg, *Atom-Photon Interactions: Basic Processes and Applications* (Wiley, New York, 1992), ISBN 9780471293361.

[23] B. Xiao, X.-K. Wang, Y.-G. Zheng, Y.-M. Yang, W.-Y. Zhang, G.-X. Su, M.-D. Li, X. Jiang, and Z.-S. Yuan, Generating two-dimensional quantum gases with high stability, Chin. Phys. B **29**, 076701 (2020).

[24] B. Yang, H. Sun, C.-J. Huang, H.-Y. Wang, Y. Deng, H.-N. Dai, Z.-S. Yuan, and J.-W. Pan, Cooling and entangling ultracold atoms in optical lattices, Science **369**, 550 (2020).

[25] B. Yang, H.-N. Dai, H. Sun, A. Reingruber, Z.-S. Yuan, and J.-W. Pan, Spin-dependent optical superlattice, Phys. Rev. A **96**, 011602(R) (2017).

[26] W.-Y. Zhang *et al.*, Functional building blocks for scalable multipartite entanglement in optical lattices, arXiv:2210.02936.

[27] S. Sachdev, K. Sengupta, and S. M. Girvin, Mott insulators in strong electric fields, Phys. Rev. B **66**, 075128 (2002).

[28] P. Fendley, K. Sengupta, and S. Sachdev, Competing density-wave orders in a one-dimensional hard-boson model, Phys. Rev. B **69**, 075106 (2004).

[29] E. Rico, T. Pichler, M. Dalmonte, P. Zoller, and S. Montangero, Tensor Networks for Lattice Gauge Theories and Atomic Quantum Simulation, Phys. Rev. Lett. **112**, 201601 (2014).

[30] C. Weitenberg, M. Endres, J. F. Sherson, M. Cheneau, P. Schauss, T. Fukuhara, I. Bloch, and S. Kuhr, Single-spin addressing in an atomic Mott insulator, Nature (London) **471**, 319 (2011).

[31] W. S. Bakr, J. I. Gillen, A. Peng, S. Fölling, and M. Greiner, A quantum gas microscope for detecting single atoms in a Hubbard-regime optical lattice, Nature (London) **462**, 74 (2009).

[32] J. F. Sherson, C. Weitenberg, M. Endres, M. Cheneau, I. Bloch, and S. Kuhr, Single-atom-resolved fluorescence imaging of an atomic Mott insulator, Nature (London) **467**, 68 (2010).

[33] J. L. Cardy, *Finite-Size Scaling* (North-Holland, Amsterdam, 1988).

[34] K. Binder and D. W. Heermann, *Monte Carlo Simulation in Statistical Physics: An Introduction* (Springer, Cham, Switzerland, 2019).

[35] P. Francesco, P. Mathieu, and D. Sénéchal, *Conformal Field Theory* (Springer, Berlin, 2012).

[36] A. Sgarro, Informational divergence and the dissimilarity of probability distributions, Calcolo **18**, 293 (1981).

[37] J. M. Deutsch, Quantum statistical mechanics in a closed system, Phys. Rev. A **43**, 2046 (1991).

[38] M. Srednicki, Chaos and quantum thermalization, Phys. Rev. E **50**, 888 (1994).

[39] M. Rigol, V. Dunjko, and M. Olshanii, Thermalization and its mechanism for generic isolated quantum systems, Nature (London) **452**, 854 (2008).

[40] L. D'Alessio, Y. Kafri, A. Polkovnikov, and M. Rigol, From quantum chaos and eigenstate thermalization to statistical mechanics and thermodynamics, Adv. Phys. **65**, 239 (2016).

[41] H. Bernien, S. Schwartz, A. Keesling, H. Levine, A. Omran, H. Pichler, S. Choi, A. S. Zibrov, M. Endres, M. Greiner, V. Vuletić, and M. D. Lukin, Probing many-body dynamics on a 51-atom quantum simulator, Nature (London) **551**, 579 (2017).

[42] C. J. Turner, A. A. Michailidis, D. A. Abanin, M. Serbyn, and Z. Papić, Weak ergodicity breaking from quantum many-body scars, Nat. Phys. **14**, 745 (2018).

[43] C. J. Turner, A. A. Michailidis, D. A. Abanin, M. Serbyn, and Z. Papić, Quantum scarred eigenstates in a Rydberg atom chain: Entanglement, breakdown of thermalization, and stability to perturbations, Phys. Rev. B **98**, 155134 (2018).

[44] F. M. Surace, P. P. Mazza, G. Giudici, A. Lerose, A. Gambassi, and M. Dalmonte, Lattice Gauge Theories and String Dynamics in Rydberg Atom Quantum Simulators, Phys. Rev. X **10**, 021041 (2020).

[45] Y. Cheng, S. Liu, W. Zheng, P. Zhang, and H. Zhai, Tunable confinement-deconfinement transition in an ultracold-atom quantum simulator, PRX Quantum **3**, 040317 (2022).

[46] R. Islam, R. Ma, P. M. Preiss, M. Eric Tai, A. Lukin, M. Rispoli, and M. Greiner, Measuring entanglement entropy in a quantum many-body system, Nature (London) **528**, 77 (2015).

[47] D. Bluvstein, H. Levine, G. Semeghini, T. T. Wang, S. Ebadi, M. Kalinowski, A. Keesling, N. Maskara, H. Pichler, M. Greiner, V. Vuletić, and M. D. Lukin, A quantum processor based on coherent transport of entangled atom arrays, Nature (London) **604**, 451 (2022).

[48] G. Magnifico, M. Dalmonte, P. Facchi, S. Pascazio, F. V. Pepe, and E. Ercolessi, Real time dynamics and confinement in the $\mathbb{Z}_n$ Schwinger-Weyl lattice model for $1+1$ QED, Quantum **4**, 281 (2020).

[49] D. Banerjee, M. Dalmonte, M. Müller, E. Rico, P. Stebler, U.-J. Wiese, and P. Zoller, Atomic Quantum Simulation of Dynamical Gauge Fields Coupled to Fermionic Matter: From String Breaking to Evolution After a Quench, Phys. Rev. Lett. **109**, 175302 (2012).

[50] F. Hebenstreit, J. Berges, and D. Gelfand, Real-Time Dynamics of String Breaking, Phys. Rev. Lett. **111**, 201601 (2013).

[51] Y. P. Huang, D. Banerjee, and M. Heyl, Dynamical Quantum Phase Transitions in U(1) Quantum Link Models, Phys. Rev. Lett. **122**, 250401 (2019).

[52] T. V. Zache, N. Mueller, J. T. Schneider, F. Jendrzejewski, J. Berges, and P. Hauke, Dynamical Topological Transitions in the Massive Schwinger Model with a θ Term, Phys. Rev. Lett. **122**, 050403 (2019).

[53] J. C. Halimeh, I. P. McCulloch, B. Yang, and P. Hauke, Tuning the topological θ-angle in cold-atom quantum simulators of gauge theories, PRX Quantum **3**, 040316 (2022).

[54] R. Ott, T. V. Zache, F. Jendrzejewski, and J. Berges, Scalable Cold-Atom Quantum Simulator for Two-Dimensional QED, Phys. Rev. Lett. **127**, 130504 (2021).